Study of the Fluid Mechanics of Transitional Steady and Pulsed Impinging Jets Using A High-Speed PIV System

H. Medina*

Centre of Excellence for Integrated Aircraft Technology, School of Mechanical and Aeronautical Engineering,
The Queen's University of Belfast, Belfast, BT9 5AH, United Kingdom

E. Benard †

Department of Aerospace Engineering, University of Glasgow, Glasgow, G12 8QQ, United Kingdom

J.C. Huang‡

Centre of Excellence for Integrated Aircraft Technology, School of Mechanical and Aeronautical Engineering,
The Queen's University of Belfast, Belfast, BT9 5AH, United Kingdom

S. Raghunathan§

Centre of Excellence for Integrated Aircraft Technology, School of Mechanical and Aeronautical Engineering,
The Queen's University of Belfast, Belfast, BT9 5AH, United Kingdom

An experimental investigation was carried out in order to study the fluid mechanics of pulsating transitional jets. The distance between the nozzle exit and the impinging plate was kept constant an equal to $H/d = 3$. The Reynolds number was also kept constant at approximately $Re = 4200$. Three pulsating frequencies were examined $St \approx 0.1, 0.25$ and 0.5. In addition, a steady impinging jet was also studied in order to provide a baseflow for comparison. It was found that the presence of a pulsation significantly affects the flow field of impinging jets, in particular, the distribution of the Reynolds stresses ($u'v'$), especially, for the jet pulsed at the highest frequency ($St = 0.5$), which exhibits a distribution of the Reynolds stresses similar to that of steady jets at much higher Reynolds numbers. It was also found that the presence of a pulsation widens the jet and leads to larger values of the radial velocity component near the impinging wall as the Strouhal number is increased.

Nomenclature

d	Nozzle diameter, m
H	Nozzle-to-plate spacing, m
Re	Reynolds number
r	Radial distance from stagnation point, m
St	Strouhal number
T_{avg}	Average temperature $(T_1 + T_2)/2$, °C
T_r	Room temperature, °C
T_1	Experiment start temperature, °C
T_2	Experiment start temperature, °C
U_e	Time-averaged centreline exit velocity, m/s
u, v	Instantaneous axial and radial velocity components, m/s

*Research Assistant, Centre of Excellence for Integrated Aircraft Technology, Non-member
†Senior Lecturer, Dept. of Aerospace Engineering, University of Glasgow, Member AIAA
‡Research Fellow, Centre of Excellence for Integrated Aircraft Technology, Member AIAA
§Bombardier-Royal Academy Chair, Associate Fellow AIAA

u', v' Mean axial and radial turbulent velocity components, m/s
x Axial distance from nozzle exit, m

Subscripts
max Cycle maximum velocity
min Cycle minimum velocity
rms Root mean square
Abbreviations
PIV Particle image velocimetry
TKE Turbulent kinetic energy

I. Introduction

Jets generate a type of flow which consists of a fluid being discharged from a nozzle, whether it is an orifice, a slot, a round nozzle, a contracting nozzle, etc. into an ambient fluid. This type of jet is called a free-jet. However, when a surface is placed in such a way that the development of the jet is interrupted, an impinging jet is created. Impinging jets are characterised by a rapid deceleration of the discharged fluid as it reaches the surface. This deceleration leads to high rates of momentum, heat and mass transfer, consequently, impinging jets have found a place in many industrial applications. For example, cooling of electronics, cooling of the inner surfaces of turbine blades, etc.

Due to the numerous practical applications of impinging jets, their study has been mainly oriented towards understanding their mass, momentum and heat transfer characteristics[1,2]. However, they are also significant from an academic point of view, since they offer a simple configuration for the study of both, free shear layers and boundary layers. Furthermore, they are also important from a modelling point of view, since turbulence models are mostly tested on flows that are parallel to a wall, therefore, there are not equipped to deal with impinging flows whose streamlines are are not parallel to the wall. Even though efforts to improve computational models have been made, they are being held back by the lack of detailed experimental data[3] because research on impinging jets is still mainly oriented towards understanding the heat transfer characteristics of impinging jets at high Reynolds numbers since they lead to the highest rates of heat transfer. In addition, due to the many different configurations for jet impingement, there are often contradictions observed in the literature.[4] Interestingly, when impinging jets are pulsated, there is evidence that suggests that heat transfer can be enhanced in comparison to steady jets[5,6] but similarly to steady impinging jets, this evidence is also contradictory, given that the literature on the heat transfer characteristics of pulsed jets also show a deterioration of heat transfer in the presence of pulsation.[7] In addition, research on pulsating impinging and jets has also concentrated on heat transfer, and the velocity and turbulent fields have been mostly ignored. There are only a few works available that study the velocity field of pulsed jets[8,9] However, these studies only consider either laminar or turbulent pulsating jets, but are also still mainly devoted to the understanding of heat transfer, and therefore, only present limited velocity data. Finally, it is evident that due to the large number of potential experimental configurations, and the contradictions observed throughout the literature for both steady and pulsating jets, there is a need for both, a systematic approach to the study of impinging jets, and also an in-depth study of the flow field and fluid mechanics. This can not only serve as a basis to understanding how the velocity field might affect heat transfer, but also to provide data for turbulence model validation.

II. Experimental Facility

A custom built water facility was used to carry out the experimental programme. This facility operates on a recirculating principle. It relies on a gravity fed mechanism to generate the jet. An overhead tank is used in order to provide the head needed. The water passes through the pulsator (the valve remains fully opened for the steady jet experiments) and the nozzle inlet, then it finally exits at the test section into the main water tank. The excess water from the main tank is collected into a reservoir tank, from there, the water is pumped back up to the overhead tank. A constant water level in the head tank is necessary in order to keep a steady supply of water to the test section, therefore, an overflow was put in place, the water from the overflow is sent to the reservoir tank. For an overview of the experimental apparatus see figure 1.

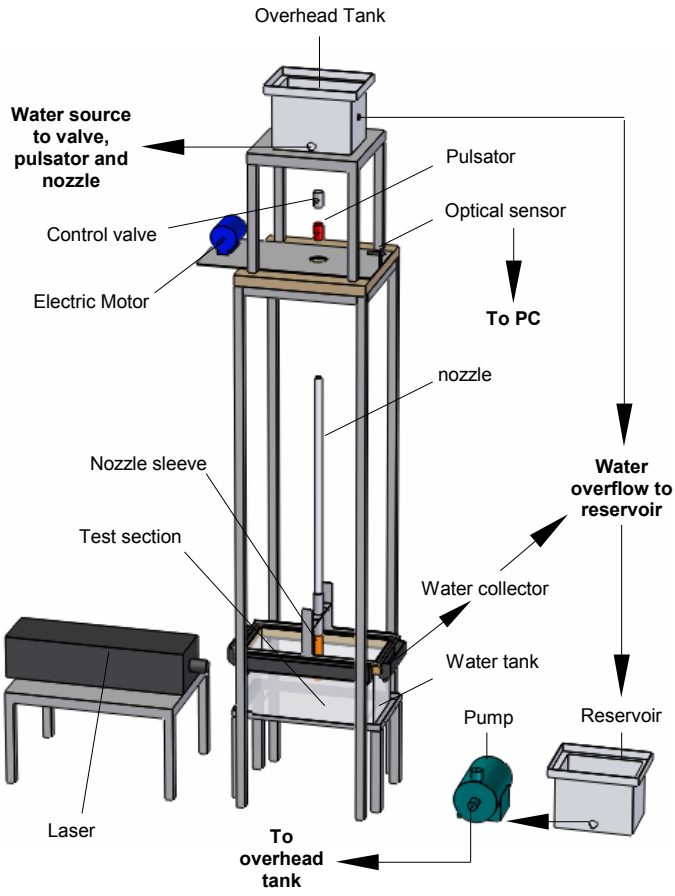

Figure 1. Experimental Facility Overview

A. Major Components

1. Water Tank

The main tank, which contains the test section, was a rectangular glass tank. Glass was a convenient material because it allows visual access to the test section. The inner dimensions of the tank were 605.6mm long, 302.8mm tall and 300.8mm wide. The glass thickness was 2mm. This tank is capable of holding approximately 55 litres of water.

2. Nozzle

In order to ensure a fully developed exit profile, a round nozzle of 50 diameters in length was utilised. The first 40 diameters(1,220mm) consist of a straight PVC tube. However, for the last 10 diameters (305mm) of the nozzle a sleeve was used to ensure that the inner section of the nozzle remained circular. Since water was used as the working fluid, the material of the nozzle chosen was PVC in order to prevent rusting of the nozzle and maintain the inner wall of the nozzle smooth. Finally, the inner diameter of the nozzle was 30.5mm.

3. Pulsator

In order to pulsate the flow a custom-built pulsator was utilised. The pulsator is make up from three main components, namely, a rotating valve, a reduction mechanism, and a driving motor. A PB100 (PN25)

chromium-plated brass full bore valve was modified so that it could rotate 360 degrees. Therefore, interrupting the water flow and leading to a pulsation (two pulses per revolution). This valve was chosen for two main reasons, firstly, it is water tight, secondly, it is also air tight, this prevents air from entering the water flow, therefore, preventing the formation of bubbles. The valve had a bore of $25mm$. Finally, the rotating valve was driven using an ABB motor (model M2VA71B-2) rated at 0.55 Kw of power. This 3 phase motor was controlled using a control unit also manufactured by ABB. Once a rotating frequency was selected it was kept constant within 0.1 Hz. The maximum frequency at which the motor could be rotated was 47.5 Hz, which translates to a maximum rotating frequency of 2.8 Hz for the valve due to the presence of the reduction mechanism.

III. Experimental Programme

Particle image velocimetry was the technique used to acquire the velocity data. The main advantage of this technique is that it provides quantitative velocity information of the flow field being studied in a non-intrusive manner. The flow is seeded with small particles, which must match the density of the fluid so that they follow the flow accurately. The velocity data is obtained by acquiring two images of the flow field at a known time interval, then, the images are divided into interrogation windows and the average particle displacement is calculated using complex cross-correlating algorithms.

A. Data Acquisition

A high-speed PIV system was used in order to acquire time-resolved velocity data. This system is comprised of a laser head, a power supply unit, a chiller (used to cool the laser head), a high-speed camera and a PC. Both the laser head and the power supply unit are manufactured by Lightwave Electronics. The laser head consists of a Nd:YAG laser which produces pulses of a wavelength of 532 nm at a maximum power of 100 mW. The system can be triggered internally and externally. If the system is triggered internally it can be operated at frequencies of up to 100 KHz, when triggered externally, it can operate up to 16 KHz. In order to maintain the highest possible camera resolution, the maximum operating frequency chosen was 500 Hz. The camera used to capture the images was a HSS-2 HighSpeedStar Video Camera System provided by LaVision. This is single frame CCD digital camera with a storage capacity of 1.28 GB (1022 images at highest resolution). It has a spatial resolution of 1280 pixels by 1024 pixels. The images capture by the camera were then stored in a PC for post-processing and analysis. The PC controls the acquisition process by synchronising the various components of the PIV system. It also provided the trigger for the steady experiments. The TTL trigger for the pulsed experiments was provided by an optical sensor (Monarch Instrument, Model ROS-5W) pointed at the rotating valve. This sensor is needed so that the images for the pulsed experiments can be taken at the same point in the cycle with an accuracy of 0.005%.

1. Software and Calibration

The software used (Davis 7.0) plays a fundamental role in the image acquisition process, as well, as image post-processing. The software oversees the overall acquisition process by providing timing rules and trigger synchronisation. Therefore, it ensure that the acquisition of the images is accurate. In addition, this software is also used for the spatial calibration of the camera. The calibration process assigns a physical length scale (mm) to each camera pixel, also, it minimises image distortions by calculating a mapping function. This mapping function provides a correlation between the image captured by the camera and the corrected image which is calculated by eliminating the distortion present in a calibration plate. The calibration plate used to calibrate the camera was a $80mm$ x 80 mm laminated card. It had a white background with 225 black crosses. The distance between crosses was 5 millimetres. Once the camera is calibrated, the system is ready to acquire the images. After the acquisition of the images, the software was used to extract the velocity data. The velocity data is extracted by examining two consecutive images and calculating the distance traveled by particles in the flow within one interrogation window. The choice of interrogation window and post-processing was the same for all experiments. A multi-pass (2) decreasing window size algorithm with a 50% overlap was used. The initial interrogation window size was 128x128 pixels and the final window size was 32x32 pixels. Thanks to the use of window overlapping, the final spatial resolution is 16 pixels.

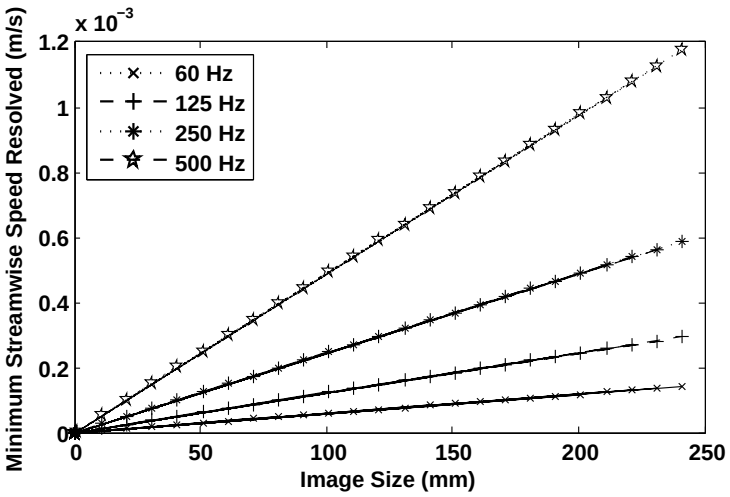

Figure 2. System accuracy for streamwise velocity component (1028 pixels)

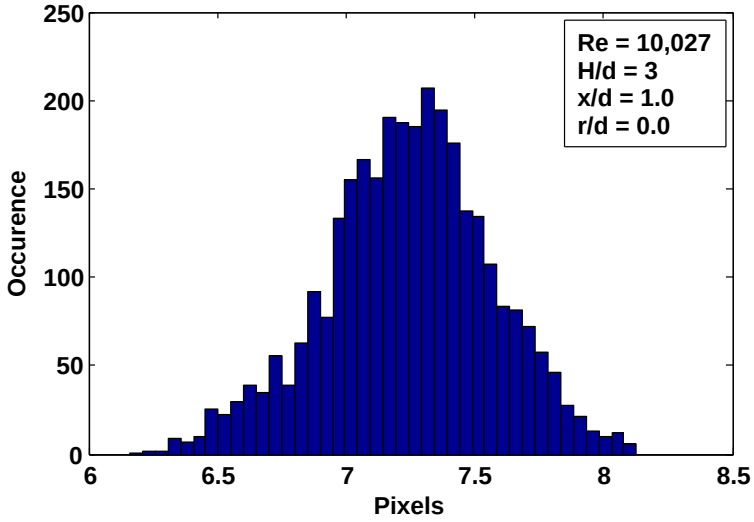

Figure 3. Typical displacement histogram at $x/d = 1$ and $r/d = 0$ for $H/d = 3$ and $Re = 10000$

With the aid of sub-pixel estimators used by the software, the PIV system is capable of measuring displacements as small as 0.1 pixel. Therefore, the minimum resolved speed is a function of the camera magnification and the acquisition frequency as shown in figure 2. Based on the highest acquisition frequency and the largest field of view employed, the system accuracy is $\pm 0.001\ m/s$. There are many factors that can lead to errors in the calculation of the velocity vectors. These include; the choice of particle, out-of-plane motion, high displacement gradients, laser accuracy, peak-locking, etc. By an appropriate selection of particles (size and density) most of the potential sources of errors can be eliminated or neglected. For this particular work, the diameter of the particles was a concern since it is smaller than 2 pixels, therefore, increasing the chance of peak-locking, however, the software eliminates peak-locking since it utilises anti-peak-locking algorithms. This is evident when the displacement histogram for a typical set of results is examined as shown in figure 3. Also, a feature of the software used is that the vectors can be calculated using decreasing window sizes and overlapping, therefore, the bias towards small particle displacements in areas with high velocity gradients is significantly reduced or even eliminated. Consequently, it was determined

that the main source of error in the velocity calculation originated from the calibration of the camera. In regards to the position of the crosses in the calibrating plate, the least accurate mapping function for the experiments carried out in this investigation gave a standard deviation of 0.2 pixel. Assuming a normal distribution of the crosses, and for a 95% confidence level, a given interrogation window will be located within 0.4 pixel of its measured position. Therefore, for a final interrogation window of 32x32 pixels, the estimated error is ±1.25%.

B. Data Analysis

Once the velocity data were extracted from the acquired images using Davis 7.0, any further analysis on the data was perform using Matlab. The velocity statistics for the steady jet were obtained using the well known Reynolds decomposition. However, for the pulsed regime, the velocity statistics were obtained using a triple decomposition of the velocity signal.

1. Reynolds Decomposition

The velocity statistics for steady jets were obtained using the Reynolds decomposition of the velocity signal shown in equation (1), where $u_{(x,r)}$ represents the measured velocity, at axial location x, and radial location r, $U_{(x,r)}$ is the local mean of the velocity signal, and $u'_{(x,r)}$ is the fluctuating part of the velocity component. Furthermore, the turbulent part of the velocity signal can be extracted rearranging equation (1), to obtain equation (2). Using this relation, the turbulent statics can be computed at each position (x, r), over the entire data range, N, using the equations shown in table 1, where N, is the number of vector fields. Finally, the time between vector fields corresponds to $1/f$, where f, is the acquisition frequency.

$$u_{(x,r)} = U_{(x,r)} + u'_{(x,r)} \tag{1}$$

$$u'_{(x,r)} = u_{(x,r)} - U_{(x,r)} \tag{2}$$

Statistic Type	**Equations**
Velocity Fluctuations	$u'_{rms(x,r)} = \sqrt{\frac{1}{N}\sum_{i=1}^{N}\left(u_{i(x,r)} - U_{(x,r)}\right)^2}$
Mean TKE	$k_{(x,r)} = \frac{1}{2N}\sum_{i=1}^{N}\left(u_{i(x,r)} - U_{(x,r)}\right)^2 + \left(v_{i(x,r)} - V_{(x,r)}\right)^2$
Reynolds Stresses	$u'v'_{(x,r)} = \frac{1}{N}\sum_{i=1}^{N}\left(u_{i(x,r)} - U_{(x,r)}\right)\left(v_{i(x,r)} - V_{(x,r)}\right)$

Table 1. Turbulent quantities equations used for steady jets

2. Triple Decomposition

The velocity signal of the pulsed jets was decomposed using a triple decomposition[10,11] shown in equation (3), where $u_{(x,r)_t}$ is the total velocity or measured velocity, $U_{(x,r)}$ is the time-averaged velocity over all the cycles, $\widetilde{U}_{(x,r)_t}$ is the phase-locked averaged velocity, measured from $U_{(x,r)}$, and finally, $u'_{(x,r)_t}$ is the turbulent or fluctuating component. In addition, x and r, represent the axial and radial locations where the velocity signal is extracted, at time t. In order to reduce computing time, the time-averaged velocity $U_{(x,r)}$, which has a fixed value over time, was combined with the phase-locked average velocity $\widetilde{U}_{(x,r)_t}$ resulting in $\widehat{U}_{(x,r)_t}$, therefore, equation (3), can be rewritten as shown in equation (4), which represents a dual decomposition of the velocity signal. Finally, the turbulent component of the velocity signal can be extracted using equation (5). This process is shown graphically in figure 4. Therefore, $u'_{(x,r)_t}$, represents the turbulent part of the velocity signal at time t of the cycle, but with the cyclic component removed. The relations used in order

to calculated the turbulent quantities for pulsed jets are shown in table 2, where N is the total number of velocity fields and t_i represents the time in the cycle that corresponds to a given value of N.

$$u_{(x,r)_t} = U_{(x,r)} + \widetilde{U}_{(x,r)_t} + u'_{(x,r)_t} \tag{3}$$

$$u_{(x,r)_t} = \widehat{U}_{(x,r)_t} + u'_{(x,r)_t} \tag{4}$$

$$u'_{(x,r)_t} = \widehat{U}_{(x,r)_t} - u_{(x,r)_t} \tag{5}$$

Statistic Type	Equations
Velocity Fluctuations	$u'_{rms(x,r)} = \sqrt{\frac{1}{N}\sum_{i=1}^{N}(u_{i(x,r)_{t_i}} - \widehat{U}_{(x,r)_{t_i}})^2}$
Triple Correlations	$u'^3_{(x,r)} = \frac{1}{N}\sum_{i=1}^{N}(u_{i(x,r)_{t_i}} - \widehat{U}_{(x,r)_{t_i}})^3$
Mean TKE	$k_{(x,r)} = \frac{1}{2N}\sum_{i=1}^{N}(u_{i(x,r)_{t_i}} - \widehat{U}_{(x,r)_{t_i}})^2 + (v_{i(x,r)_{t_i}} - \widehat{V}_{(x,r)_{t_i}})^2$
Reynolds Stresses	$u'v'_{(x,r)} = \frac{1}{N}\sum_{i=1}^{N}(u_{i(x,r)_{t_i}} - \widehat{U}_{(x,r)_{t_i}})(v_{i(x,r)_{t_i}} - \widehat{V}_{(x,r)_{t_i}})$

Table 2. Turbulent quantities equations used for pulsed jets

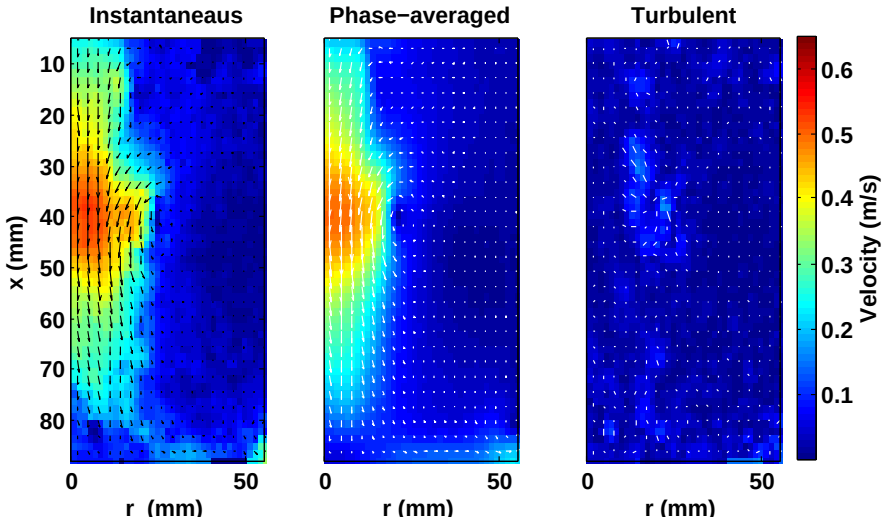

Figure 4. Decomposition of the velocity signal (whole-field)

3. Experimental Error and Uncertainty

Table 3 presents a summary of the estimated error for the various turbulent statistics presented in this work. As already mentioned, the accuracy of the velocity measurements is based on the most limiting experiments carried out, giving an accuracy of 0.001 m/s. Also, the estimated error on the instantaneous and time-averaged velocity measurements was estimated at $\pm 1.25\%$.

Experimental Quantity	Associated Error
instantaneous velocities (u, v)	$\pm$1.25%
mean velocities (U, V)	$\pm$1.25%
turbulent components (u', v')	$\pm$2.00%
velocity fluctuations (u'_{rms}/U_e, v'_{rms}/U_e)	$\pm$3.00%
Reynolds stresses ($u'v'/U_e^2$)	$\pm$4.50%
TKE (k/U_e^2)	$\pm$5.50%

Table 3. Error summary

Variables			Temperatures (°C)				Acquisition Information		Exit Conditions			
Re	H/d	St	T_r	T_1	T_2	T_{avg}	Freq. (Hz)	No. Imgs.	U_{min}	U_{max}	U_e	A_N
4000	3	-	19.00	20.00	20.20	20.10	250	3066	-	-	0.129	-
3800	3	0.11	17.50	16.50	17.40	16.95	60	6840	0.079	0.170	0.135	20%
4800	3	0.23	18.10	19.90	20.30	20.10	125	6825	0.120	0.204	0.157	20%
4315	3	0.47	19.90	20.20	20.70	20.45	250	10710	0.083	0.241	0.140	40%

Table 4. Test conditions summary; velocities in m/s

IV. Results and Discussion

A. Flow Characterisation

1. Axisymmetry

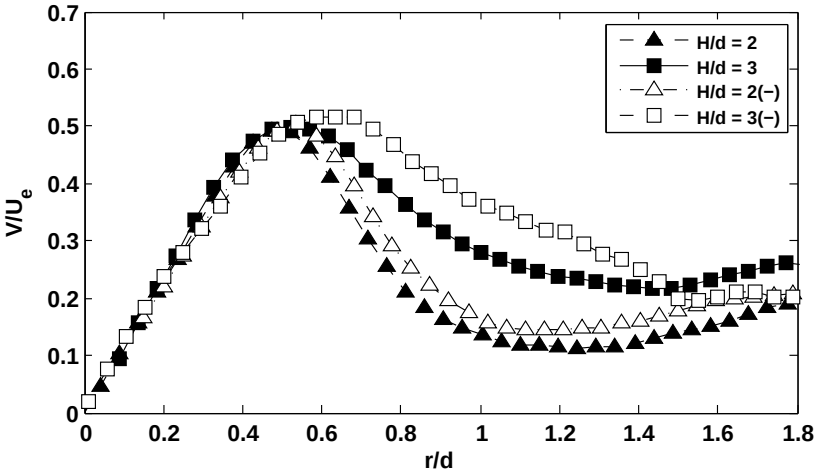

Figure 5. Mean radial velocity component near the impinging wall for different Reynolds numbers; (-) represents left-hand side of the profile which has been folded ($x/d = 2.85$, $H/d = 3$)

A round nozzle was used in order to provide an axisymmetric jet flow. Also, in order to ensure that the jet was axisymmetric on impingement, the water tank was built with adjustable legs so that the impinging surface was parallel to the floor. In addition, the nozzle was securely fixed by a transverse fixture holding it in place at the centre of the water tank. Attempts were made to test for axisymmetry, however, due to limitations inherent to the PIV system used (laser power), it was only possible to check for symmetry on the plane where the laser sheet was originally designed to be located. Figure 5 shows the radial velocity component near the impinging wall for two nozzle-to-plate spacings, $H/d = 2$ and $H/d = 3$. It can be seen that there is good symmetry for the jet with the lower H/d, however, for $H/d = 3$, there is a slight break in symmetry near the impinging wall for $0.6 < r/d < 1.4$ with a maximum deviation of approximately 18%. This break in symmetry is attributed to laser light reflections present in the near wall region on the left-hand side of the test section which impaired the calculation of the velocity vectors.

2. Exit Conditions

The experimental rig was designed to generate impinging jets with a fully developed exit velocity profile. For the steady flow regime, the velocity profiles at exit were fully developed for Reynolds numbers greater than 3,250. On the other hand, for the pulsed flow regime, the exit velocity profiles were fully developed for Reynolds numbers greater than 3,500. Figure 6 shows the exit velocity profiles at 0.5 diameters away from the nozzle exit for three different Reynolds numbers. As it can be observed, these exit velocity profiles are fully developed.

The axial velocity fluctuations at the jet centreline and at 0.5 diameters away from the nozzle exit are shown in figure 7 for different Reynolds numbers. The results of Aydore[12] and Gardon[13] are also shown for comparison. The correlation shown in figure 7 closely fits the values of the velocity fluctuations within the free jet region of impinging jets. This correlation holds for Reynolds numbers ranging from 3500 (transitional) to 15000, as long as $H/d > 3$. The correlation to include jets with higher Reynolds numbers would not be a simple straight line because for $Re > 20000$ the value of u'_{rms}/U_e tends to an asymptotic value of 0.01.[14,15] Finally, the phase-averaged velocity characteristics at the jet centreline and at $x/d = 0.5$ is shown if figure 8.

B. Effect of the Strouhal Number

The effect of the non-dimensional frequency, St, on the flow field of transitional ($Re \approx 4200$) and pulsating ($0.10 < St < 0.50$) impinging jets will be presented. The flow field of a steady and transitional impinging jet will be used for comparison. All the other factors that affect the flow field were kept constant ($Re \approx 4200$, $d = 30mm$ and $H/d = 3$).

1. Time-Averaged Velocity Field

Firstly, the effect of the Strouhal number on the time-averaged flow field is shown if figure 9. This figure shows that the jet becomes wider with the presence of a pulsating frequency at $x/d > 0.5$. Also, the wall jet becomes stronger with increasing the Strouhal number. This indicates that the presence of a pulsation has a considerable effect on the flow field of impinging jets. For instance, the centreline mean axial velocity decay for the various values of St is shown in figure 10. It shows that the centreline velocity decays more rapidly as St is increased, also, it decreases more rapidly than steady jets. For example, up to $x/d \approx 2.5$, pulsed jets exhibit a similar reduction of the centreline axial velocity component (20%), however, for the steady jet, the centreline velocity exhibits a reduction of 20% at $x/d \approx 2.55$.

The development of the jet in the axial and radial direction is also affected by the pulsation, as shown in figure 11. For instance, near the nozzle exit (figure 11c), the radial profiles of the mean axial velocity component (left) for pulsating jets indicate that the jet becomes wider in the presence of a pulsation. figure 11c shows the presence of a local minimum and maximum in the radial profiles of the mean radial component which increase in magnitude as the Strouhal number is increased. Further downstream, at $x/d = 2.5$, a more rapid spread of the jet as the frequency is increased is evident. figure 11b shows that the radial profiles of the mean axial component become wider as the frequency is increased. Furthermore, the mean radial velocity component also increases as the Strouhal number is increased. This confirms that the jet spreads more rapidly as the pulsating frequency is increased. Finally, near the impinging wall (figure 11a), whereas the pulsating frequency does not have a pronounced effect on the mean axial velocity, the mean radial velocity is significantly influenced by the Strouhal number. figure 11a shows that as the pulsating frequency is increased, the mean radial velocity component also increases. This increase is particularly significant for the higher Strouhal numbers tested. The profiles of V/U_e for the higher strouhal numbers exhibit a significant increase when compared to the steady jet. However, for $St = 0.10$, there is a decrease of the radial velocity component when compared to the steady case. This increase could be attributed to the increase in vorticity experienced as the frequency is increased (figure 12). This implies that each individual vortex reaching the target wall carries more angular velocity, in addition, as the frequency is increased, such vortices reach the impinging wall more frequently leading to an increase in the mean radial velocity component and a stronger wall jet.

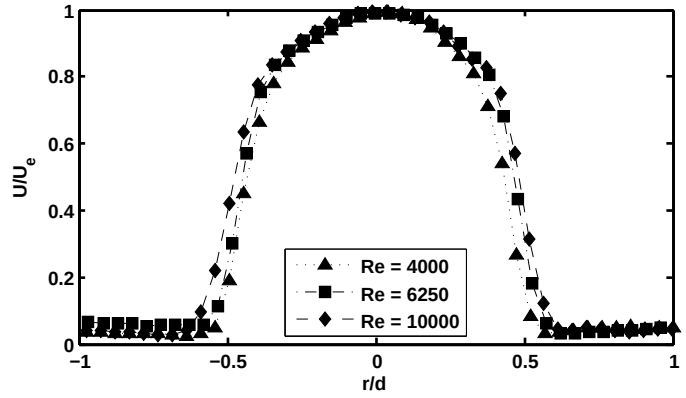

Figure 6. Exit velocity profiles at various Reynolds numbers ($x/d = 0.5$, $r/d = 0$)

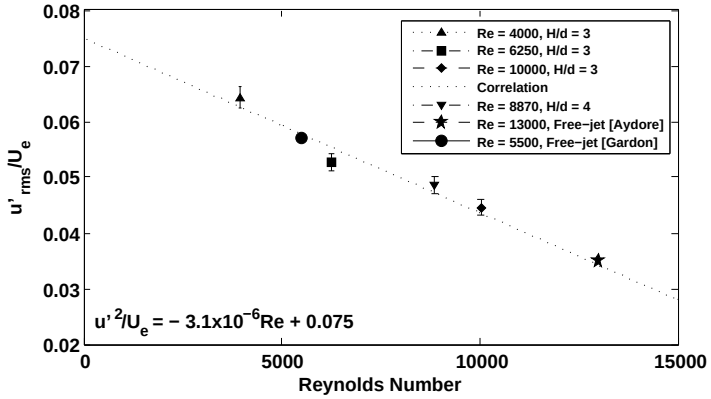

Figure 7. Axial velocity fluctuations in the free jet region ($x/d = 0.5$ and $r/d = 0$)

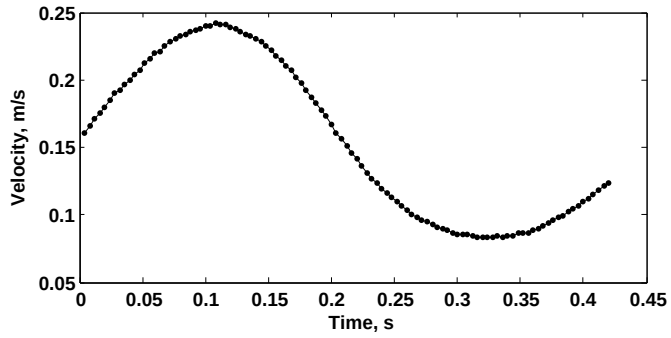

Figure 8. Phase-averaged velocity at $x/d = 0.5$ and $r/d = 0$ for the jet with $Re \approx 4200$, pulsed at $St \approx 0.5$ and placed at $H/d = 3$

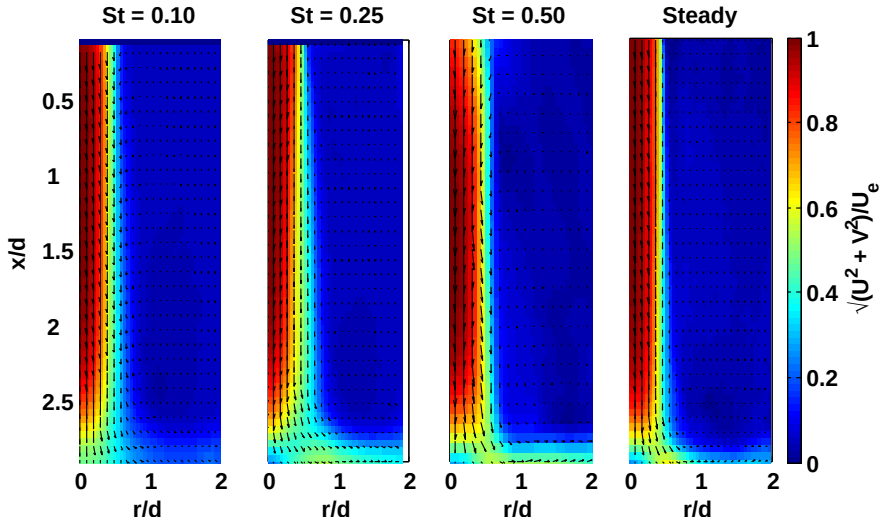

Figure 9. Effect of the Strouhal number on the time-averaged velocity field ($H/d = 3Re \approx 4200$)

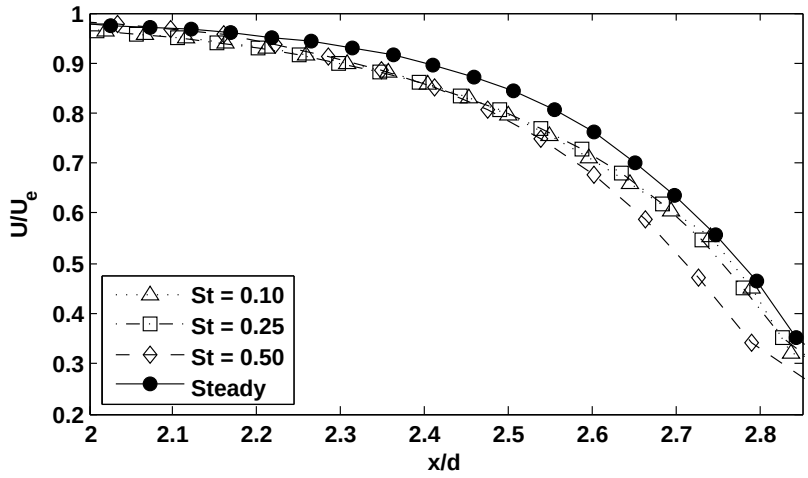

Figure 10. Centreline mean axial velocity decay ($H/d = 3Re \approx 4200$)

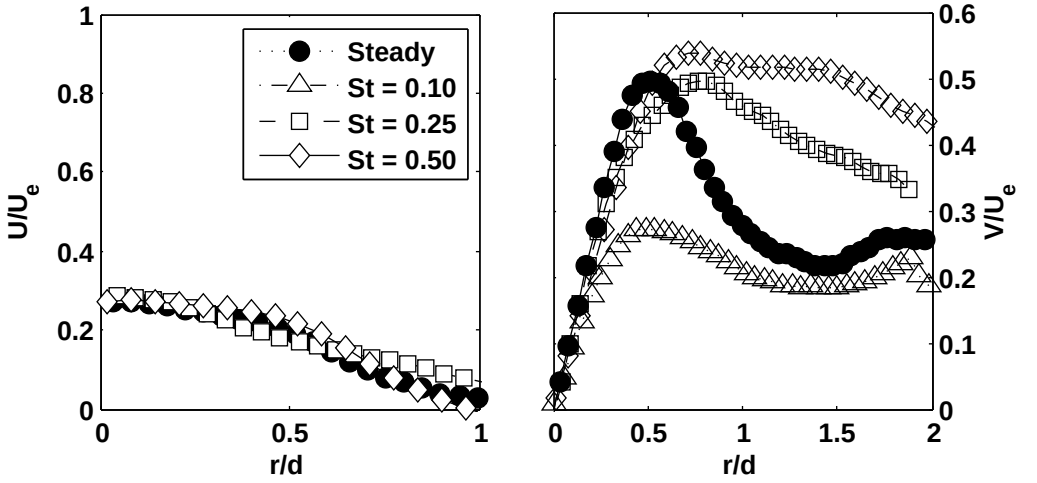

(a) x/d = 2.85

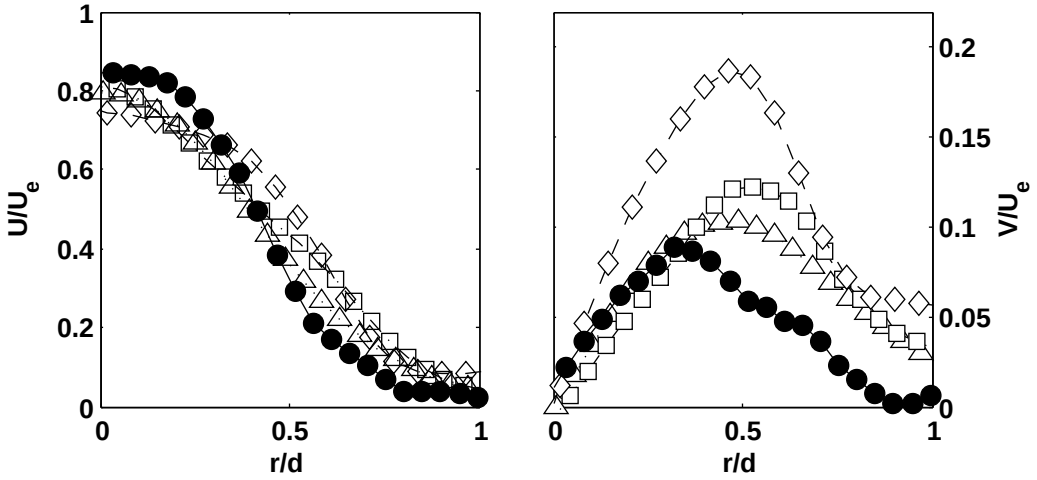

(b) x.d = 2.5

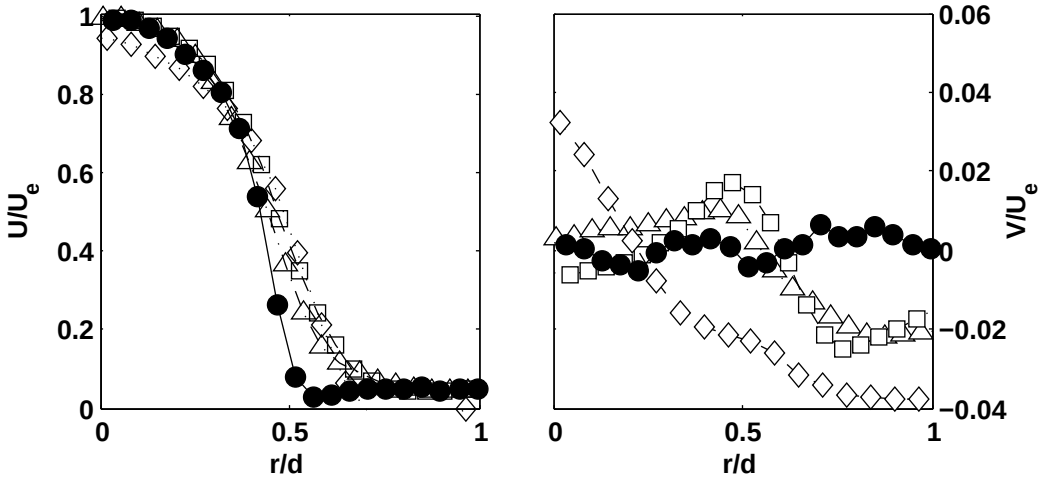

(c) x/d = 0.5

Figure 11. Radial profiles of mean axial (left) and radial (right) velocity components ($H/d = 3$, $Re \approx 4200$)

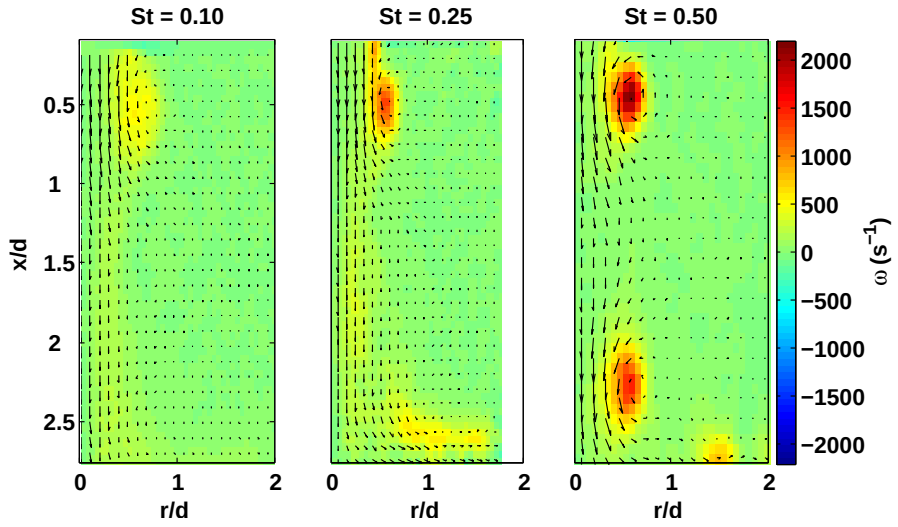

Figure 12. Effect of the Strouhal number on the vorticity field ($H/d = 3$, $Re \approx 4200$)

2. Velocity Fluctuations

Figures 13 and 14 show the effect of the Strouhal number on the radial and axial velocity fluctuations. These figures show that, overall, there is an increase in the velocity fluctuations, in both the axial and radial directions, as the Strouhal number is increased. This indicates more mixing within the shear layer of the jet as the frequency is increased. Also, both the axial and radial velocity fluctuations are larger for pulsating jets compared to steady jets, even for the lowest frequency tested.

The centreline axial velocity fluctuations are shown in figure 15. It shows that the pulsation frequency affects the development of the axial velocity fluctuations. For instance, near the nozzle exit, there is an increase in u'_{rms}/U_e for the pulsating jets when compared to the steady jet. As St increases, fluid mixing near the nozzle exit is increased. This can be attributed to more frequent fluid acceleration and deceleration cycles as St is increased. Furthermore, figure 15 also shows that for $St = 0.10$ and 0.25, the velocity fluctuations for $0.5 < x/d < 2.2$ are lower than those of the steady jet. This indicates that at these frequencies, the vortex pairs are not strong enough to affect the jet centreline. This could also be an indication that mixing is contained within the shear layer of the jet (vortices) more efficiently when the jet is pulsed at $St = 0.10$ and 0.25 than for the steady jet, at least for $0.5 < x/d < 2.2$. However, for $x/d < 2.2$ there is an increase in u'_{rms}/U_e for all pulsed jets. This increase could be a result of the distortion and break up of the vortices, leading to more mixing near the impinging wall for pulsed jets. In addition, the centreline axial velocity fluctuations near the stagnation point decrease with increasing St, probably due to a better preservation of the vortex pairs as the frequency is increased, which in turn leads to a stronger influence of the vortices on the jet centreline (see figure 12).

Figure 16 shows the profiles of the radial velocity fluctuations near the impinging wall. First of all, it can be observed that the profile for the lower frequency exhibits a trend similar to that of the steady jet since it shows an initial increase of v'_{rms}/U_e followed by a gentle decrease. However, as St is further increased this trend changes, for $St = 0.25$, the radial velocity fluctuations exhibit a steady increase, whereas, for $St = 0.5$, there is an initial increase of v'_{rms}/U_e followed by a gentle decrease and a second local maximum located at approximately $r/d = 1.3$. This second maximum could be a result of the interaction between individual pulses which leads to a local increase of v'_{rms}/U_e (see figure 12).

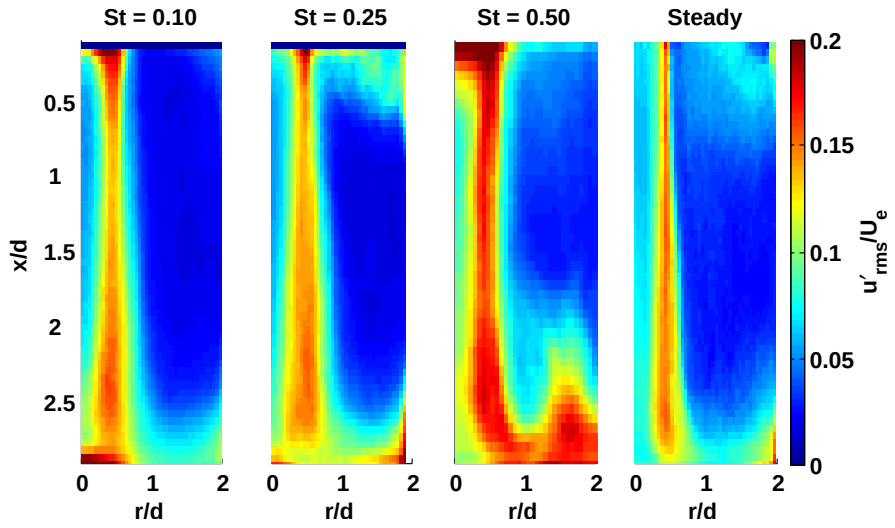

Figure 13. Axial velocity fluctuations ($Re \approx 4200$)

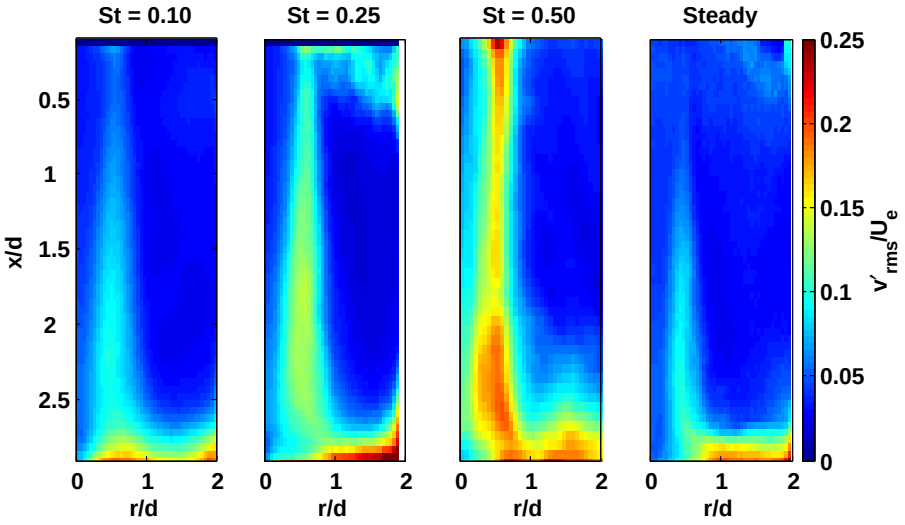

Figure 14. Radial velocity fluctuations ($Re \approx 4200$)

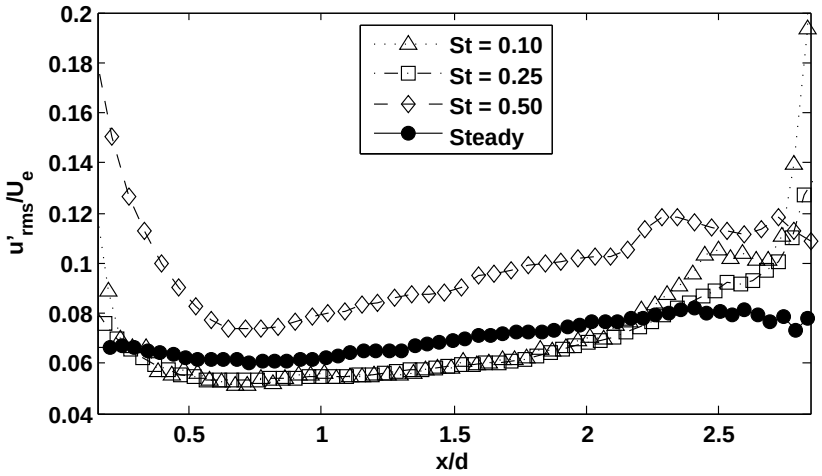

Figure 15. Centreline axial velocity fluctuations ($Re \approx 4200$)

3. Turbulent Kinetic Energy

Figure 17 shows that the mean TKE within the shear layer of the jet increases as the Strouhal number is increased. Also, the mean TKE is larger for pulsed jets than steady jets, even for the lowest frequency tested. Interestingly, for the jet pulsed at $St = 0.5$ there is marked increase of the mean TKE within the shear layer at $2 < x/d < 2.8$, this increase could be attributed to the fact that pulses reach the surface more frequently, which are also relative stronger compared to those with lower Strouhal number (see figure 12), therefore, having interacting effects with each other, while also being distorted by the impinging wall, which in turn leads to increased mixing in this region.

Figure 18 shows that the profiles of the mean TKE have different trends depending on the Strouhal number. Firstly, when the jet is pulsed at $St = 0.10$ there is an increase in the mean TKE for $0 < r/d < 0.75$ when compared with the steady case, followed by a decreased for $r/d > 0.75$, where the mean TKE reaches levels lower than that of the steady jet. Secondly, for $St = 0.25$ the mean TKE exhibits a gently increase in the radial direction, following a trend similar to that of the steady jet, however, it exhibits larger values for $r/d > 0.75$. Finally, for $St = 0.5$ the radial profile of the mean TKE exhibits two local maxima, the first located at $r/d \approx 0.6$, and the second located at $r/d \approx 1.4$. These differences in the radial profiles of the mean TKE can be attributed to both the difference in vorticity strength, and the frequency at which vortex pairs reach the target wall. For instance, for the lowest Strouhal number, the vortex pairs are rather weak and get distorted before reaching the target wall, which explains the larger values of the mean TKE at the stagnation region, in addition, they reach the target surface less frequently, which can explain the lower values of k/U_e^2 for $r/d > 0.75$. The steady increase in the mean TKE for $St = 0.25$ could be a result of relative stronger vortex pairs reaching the wall in isolation, that is, without being influenced by preceding vortices. This indicates that not only the pulsating frequency would have an effect on the interaction between vortices at the wall, but also the nozzle-to-plate spacing, and must also be considered. Finally, the presence of two local maxima in the radial profile of the jet pulsed at $St = 0.5$ could be a result of relatively stronger vortices interacting with each other near the impinging wall, leading to the development of a second maximum, whereas, the first maximum coincides with the location where the inner part[a] of the vortex pairs impinge with the wall initially (see figure 12 on page 13).

4. Reynolds Stress (u'v')

The effect of the Reynolds number on the Reynolds stresses will be presented in this section. The Reynolds stresses are a measure of the net transfer of momentum across a surface due to fluctuations in fluid velocity, they are also referred to as eddy stresses. The analysis of the Reynolds stresses presented in this study is

[a]Refers to the peripheral side of the vortex closest to the jet axis

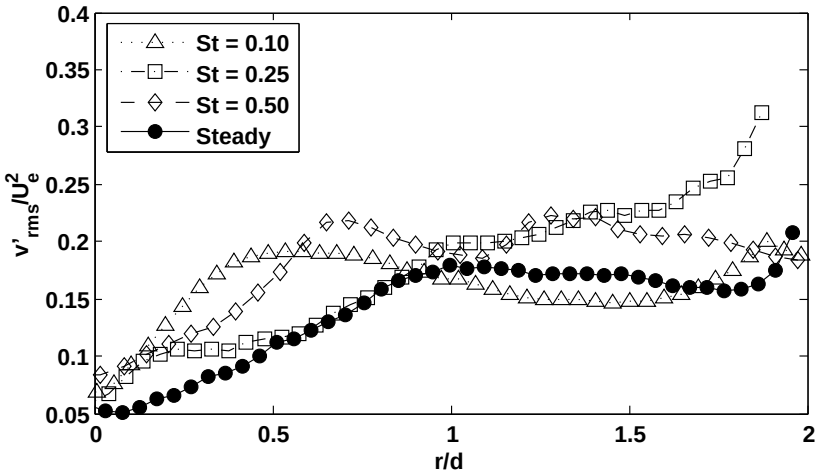

Figure 16. Radial velocity fluctuations near the impinging wall ($x/d = 2.85$)

based on the work of Wallace.[16]

The time history of the axial and radial velocity turbulent components (u' and v') at each point was examined in order to assess their contribution to the Reynolds stresses ($u'v'$). This was achieved by calculating a skew factor which was defined in equations (6) (steady) and (7) (pulsed), using the same notation as described in section III.B on page 6. The skew factor provided a measure of the influence and sign of u' and v'. Therefore, their relative influence on $u'v'$ could be readily assessed.

$$u'^3_{(x,r)} = \frac{1}{N}\sum_{i=1}^{N}(u_{i(x,r)} - U_{(x,r)})^3 \tag{6}$$

$$u'^3_{(x,r)} = \frac{1}{N}\sum_{i=1}^{N}(u_{i(x,r)_{t_i}} - \widehat{U}_{(x,r)_{t_i}})^3 \tag{7}$$

The classification of the Reynolds stresses used in this study is shown in figure 19. The notation shown makes a distinction of the Reynolds stresses by the use of lower case letters and capital letters to indicate shear layer stresses and wall jet stresses respectively. This distinction is necessary due to the fact that the flow changes direction, from the initial streamwise direction, to the wall jet region developed upon impingement. The border for the wall jet region chosen was 0.5 diameters from the wall (use of capital letters). In addition, within the shear layer, two types of Reynolds stresses were observed which are both positive. Firstly, both u' and v' being negative which is representative of entrainment (en). Secondly, both being positive which indicates turbulent expulsion (e). Within the wall jet, four distinct patterns for the Reynolds stresses are observed, two of which lead to positive values of $u'v'$, whereas, the remaining two lead to negative values. Positive values of $u'v'$ are generated when both u' and v' are either positive of negative. If u' and v' are positive they produce a sweep-type motion (S), however, if they are both negative they produce an ejecting effect (E). The two remaining types of Reynolds stresses are negative. The first is generated when u' is positive and v' negative, which are linked to low-speed fluidic interactions reflected towards the wall (W). In contrast, when u' is negative and v' positive their corresponding Reynolds stresses are linked to high-speed fluidic interaction outwards from the wall (O).

Figure 20 shows that initially, as the frequency is increased, both entrainment (en) and expulsion (e) within the shear layer increase. However, as the frequency is further increased to $St = 0.5$, there is a significant decrease in the entrainment Reynolds stresses (en), in particular for $0 < x/d < 1.5$. This reversal in the effect of the Strouhal number must occur at a pulsating frequency greater than 0.25 and it is currently being investigated.

Figure 20 also shows that near the impinging wall the Strouhal number has a strong effect on the type of Reynolds stresses and their distribution. For instance, for $St = 0.10$, the Reynolds stresses near the

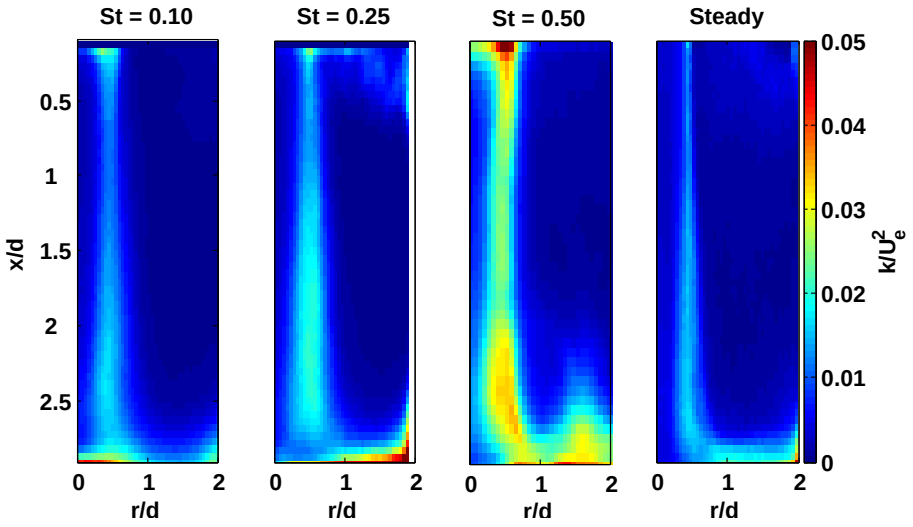

Figure 17. Mean turbulent kinetic energy ($Re \approx 4200$)

impinging wall are positive and associated with ejection (E). Also, high-speed fluidic interactions in the direction away from the wall are also present (O). However, for $St = 0.25$, Reynolds stresses associated with low-speed interaction towards the wall (W) are present, as well, as sweeping Reynolds stresses (S) just above. This indicates that as the frequency is increased from $St = 0.10$ to $St = 0.25$, the momentum transport due to the Reynolds stresses has a general tendency to act towards the impinging wall. For $St = 0.5$, and similarly to the jet pulsed at $St = 0.25$, sweeping (S) and wallwards Reynolds stresses (W) are also present, however, high-speed fluidic interactions away from the impinging wall (O) are also present at $1.5 < r/d < 2$ which indicates that momentum is initially directed towards the impinging wall, then away from it. Finally, the steady case shows that the Reynolds stresses are mainly due to high-speed fluidic interactions away from the impinging wall. It is interesting to observe that the distribution of the Reynolds stresses for the jet pulsed at $St = 0.5$ resembled that of a jet with a much higher Reynolds number (not shown in this paper). Therefore, it can be argued that the pulsating frequency would have a significant effect on the heat transfer characteristics of the jet.

V. Conclusion

The fluid mechanics of round and pulsating impinging jets have been studied. The effect of the strouhal number alone has been examined by keeping all other parameters constant. It has been found that the presence of a pulsation significantly affects the flow field of impinging jets in comparison to steady jets. First of all, pulsed jets are wider and their centreline velocity decays more rapidly, in addition, they exhibit higher turbulence intensities within the shear layer, implying that there is more mixing i.e. entrainment, which is to some extent confirmed by observing the Reynolds stress ($u'v'$). In relation to their use to enhance heat transfer, it was found that both the turbulent kinetic energy and the Reynolds stress suggest that there is more mixing present near the impinging wall for pulsed jets. However, there is also more mixing within the shear layer of pulsed jets, therefore, it could be argued that the initial thermal characteristics of pulsed jets are lost to the surrounding fluid more rapidly. This notion could explain the lower values of the Nusselt number at the stagnation point for pulsed jets in comparison to steady jets, in contrast, relative larger Nusselt numbers for pulsed jets are found in the region where the wall-jet develops, which is attributed to larger values of the turbulent kinetic energy and a change in the distribution of the Reynolds stress resembling that of jets with higher Reynolds numbers (results not shown in this paper). Finally, it became evident that there is a need to also study the effect of the nozzle-to-plate spacing since it could have an equivalent effect to that of the Strouhal number, that is, the frequency at which the vortices reach the impinging wall is affected by the nozzle-to-plate spacing. The effect of the nozzle-to-plate spacing is currently being investigated.

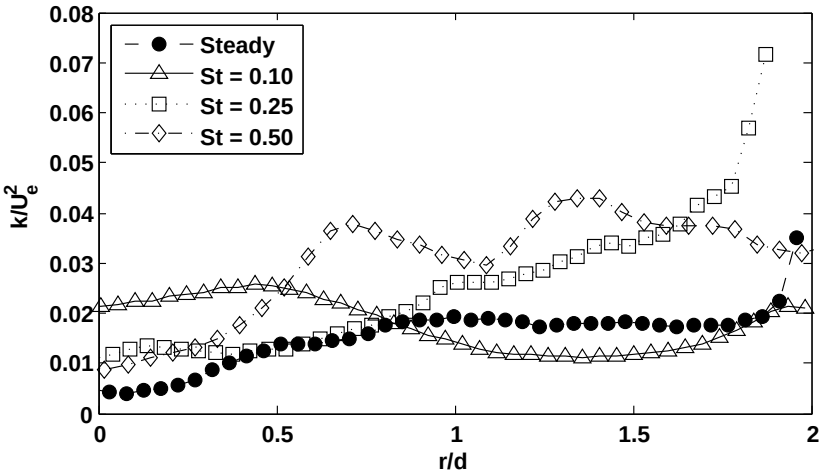

Figure 18. Mean turbulent kinetic energy near the impinging wall ($x/d = 2.85$)

References

[1]Ma, C. F., Zheng, Q., Lee, S. C., and Gomi, T., "Impingement heat transfer and recovery effect with submerged jets of large Prandtl number liquid - I. Unconfined circular jets," *International journal of heat and mass transfer*, Vol. 40, No. 6, 1997, pp. 1481–1490.

[2]Moreno, O. A., Katyl, R. H., Jones, J. D., and Moschak, P. A., "Mass transfer of an impinging jet confined between parallel plates," *IBM J. RES. Develop.*, Vol. 37, No. 2, March 1993, pp. 143–155.

[3]Nishino, K., Samada, M., Kasuya, K., and Torii, K., "Turbulence statistics in the stagnation region of an axisymmetric impinging jet flow," *International journal of heat and fluid flow*, Vol. 17, 1996, pp. 193–201.

[4]Jamabunathan, K., Lai, E., Moss, M. A., and Button, B. L., "A review of heat transfer data for single circular jet impingement," *International Journal of heat and fluid flow*, Vol. 13, No. 2, June 1992, pp. 106–115.

[5]Sailor, D. J., Rohli, D. J., and Fu, Q., "Effect of variable duty cycle flow pulsations on the heat transfer enhancement for an impinging air jet," *International journal of heat and fluid flow*, Vol. 20, 1999, pp. 574–580.

[6]Mladin, E. C. and Zumbrunnen, D. A., "Local convective heat transfer to submerged pulsating jets," *International journal of heat and mass trasfer*, Vol. 40, No. 14, 1997, pp. 3305–3321.

[7]Zvirin, Y., "Heat transfer between a pulsating impinging jet and a flat surface," *Israel journal of technology*, Vol. 5, No. 1–2, 1967, pp. 152–169.

[8]Poh, H. J., Kumar, K., and Mujumdar, A. S., "Heat transfer from a pulsed laminar impinging jet," *International communications in heat and mass transfer*, Vol. 32, 2005, pp. 1317–1324.

[9]Vejrazka, J., *Experimental study of a pulsating round impinging jet (Etude experimentale d'un jet circulaire impactant pulsant)*, Ph.D. thesis, Laboratoire des ecoulements geophysiques et industriels, Grenoble, December 2002.

[10]Hussain, A. K. M. F. and Zaman, K. B. M. Q., "Vortex pairing in circular jet under controlled excitation. Part 2. Coherent structure dynamics," *Journal of fluid mechanics*, Vol. 101, No. 3, 1980, pp. 493–544.

[11]Bremhorst, K. and Gehrke, P. J., "Measured Reynolds stress distributions and energy budgets of a fully pulsed round air jet," *Experiments in fluids*, Vol. 28, 2000, pp. 519–531.

[12]Aydore, S. and Disimile, P. J., "Natural coherent structure dynamics in near field of fully turbulent axisymmetric jet," *AIAA Journal*, Vol. 35, No. 7, July 1997.

[13]Gardon, R. and Akfirat, J. C., "The role of turbulence in determining the heat transfer characteristics of impinging jets," *International journal of heat and mass transfer*, Vol. 8, 1965, pp. 1261–1272.

[14]Ashforth-Frost, S., Jambunathan, K., Whitney, C. F., and Ball, S. J., "Heat transfer from a flat plate to a turbulent axisymmetric impinging jet," *Proc. instn. mech. engrs.*, Vol. 211, 1997, pp. 167–172.

[15]Baydar, E. and Ozmen, Y., "An experimental and numerical investigation on a confined impinging air jet at high Reynolds numbers," *Applied therman engineering*, Vol. 25, 2005, pp. 409–421.

[16]Wallace, J. M., Eckelmann, H., and Brodkey, R. S., "The wall region in turbulent shear flow," *Journal of fluid mechanics*, Vol. 54, No. 1, 1972, pp. 39–48.

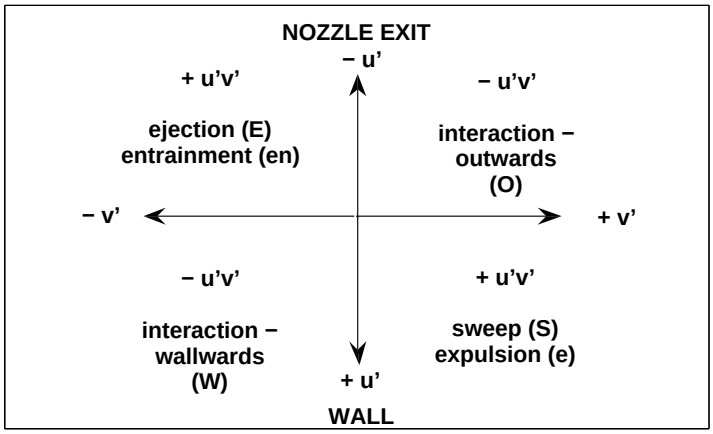

Figure 19. Sign convention and classification of the Reynolds stresses, $u'v'$

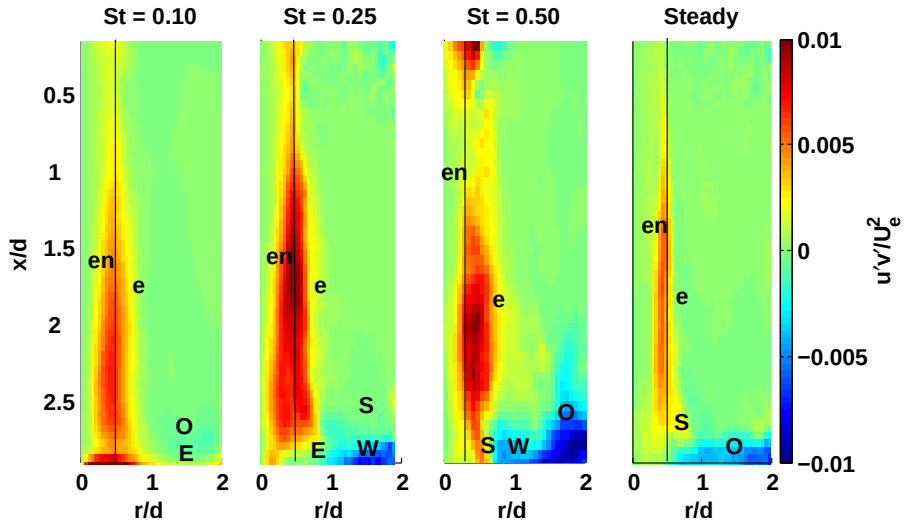

Figure 20. Reynolds stress ($u'v'$) distribution ($Re \approx 4200$)